Stellar neutron capture cross sections of ^{20,21,22}Ne

M. Heil,[1,*] R. Plag,[1] E. Uberseder,[2] R. Gallino,[3] S. Bisterzo,[3,4] A. Juseviciute,[5] F. Käppeler,[5] C. Lederer,[6] A. Mengoni,[7] and M. Pignatari[8]

[1] *GSI Helmholtzzentrum für Schwerionenforschung GmbH, Darmstadt, Germany*
[2] *University of Notre Dame, Notre Dame, USA*
[3] *Dipartimento di Fisica, Università di Torino, Via P. Giuria 1, I-10125 Torino, Italy*
[4] *INAF, Astronomical Observatory of Turin, Italy*
[5] *Karlsruhe Institute of Technology (KIT), Campus North, Institute of Nuclear Physics, PO Box 3640, Karlsruhe, Germany*
[6] *The University of Edinburgh EH9 3JZ, UK*
[7] *CERN, CH-1211 Geneva 23, Switzerland*
[8] *Department of Physics, University of Basel, Basel, Switzerland*[†]

(Dated: May 12, 2014)

The stellar (n,γ) cross sections of the Ne isotopes are important for a number of astrophysical quests, i.e. for the interpretation of abundance patterns in presolar material or with respect to the *s*-process neutron balance in red giant stars. This paper presents resonance studies of experimental data in the keV range, which had not been fully analyzed before. The analyses were carried out with the $\mathcal{R}$-matrix code SAMMY. With these results for the resonant part and by adding the components due to direct radiative capture, improved Maxwellian-averaged cross sections (MACS) could be determined. At $kT = 30$ keV thermal energy we obtain MACS values of 240 ± 29, 1263 ± 160 and 53.2 ± 2.7 μbarn for ^{20}Ne, ^{21}Ne, and ^{22}Ne, respectively. In earlier work the stellar rates of ^{20}Ne and ^{21}Ne had been grossly overestimated. ^{22}Ne and ^{20}Ne are significant neutron poisons for the *s* process in stars, because their very small MACS values are compensated by their large abundances.

I. INTRODUCTION

The astrophysical quests with respect to the neon isotopes are related (i) to the role of the ^{22}Ne$(\alpha,n)^{25}$Mg reaction as one of the major neutron sources for *s*-process nucleosynthesis and (ii) to the fact that ^{20}Ne and ^{22}Ne represent also major neutron poisons.

In Asymptotic Giant Branch (AGB) stars, ^{22}Ne is abundantly produced during He burning by successive α captures on ^{14}N, which is formed by conversion of the CNO abundances during the preceding H burning phase. An additional component of primary ^{14}N results from newly synthesized ^{12}C that is mixed to the envelope by third dredge-up and then converted to ^{14}N by H shell burning [1]. At the higher temperatures reached by the onset of He burning, the ^{14}N is transformed into ^{22}Ne by the reaction sequence ^{14}N$(\alpha,\gamma)^{18}$F$(\beta^+)^{18}$O$(\alpha,\gamma)^{22}$Ne. First (n,γ) cross section data seemed to support the poisoning effect [2], but later measurements provided evidence that this cross section is significantly smaller [3–6].

In massive stars, ^{20}Ne must be considered as a major neutron poison, because it is directly produced during C shell burning via the main channel ^{12}C(^{12}C, $\alpha)^{20}$Ne and indirectly via the reaction sequence ^{12}C(^{12}C, $p)^{23}$Na$(p,\alpha)^{20}$Ne (e.g., [7]). On the other hand, the ^{22}Ne$(n,\gamma)^{23}$Ne reaction is a relevant neutron poison already during convective core He-burning, where it competes with the ^{22}Ne(α,n) channel. ^{22}Ne becomes an even more important neutron poison in fast rotating massive stars at low metallicity, where it is made from ^{14}N of primary origin [8].

Another important aspect of the isotopic Ne abundances came to light when significantly non-solar isotope patterns characterized by almost pure ^{22}Ne were discovered in presolar grains [9, 10]. Depending on the type of carrier these grains originate from different sources. Neon embedded in SiC grains, denoted as Ne-E(H), could be ascribed to AGB stars [11, 12], whereas the Ne-E(L) component, made of almost pure ^{22}Ne, is carried by a subclass of graphite grains, especially those called "low-density graphite grains", which are mainly of supernova (Type II) or nova origin [13]. Because neutron capture nucleosynthesis is going on at all these sites, reliable (n,γ) cross sections for the Ne isotopes are crucial for the interpretation of the respective abundance patterns, in particular with respect to the strong ^{22}Ne enrichments found in these samples.

For the Ne-E(H) component it has been noted [14] that it can be reproduced by carbon stars of Population I, with solar to half-solar metallicity. In these models one finds a small nucleosynthetic production of ^{21}Ne, which is determined by neutron captures on ^{20}Ne. This production path of ^{21}Ne is important with respect to a radiogenic origin, which has been discussed to derive a cosmic-ray exposure age of the SiC grains [15, 16].

The origin of Ne-E(L) [17] relates to the production of ^{22}Na in the C-burning zone of massive stars via ^{21}Ne$(p,\gamma)^{22}$Na. This production is fueled by ^{21}Ne and protons coming from ^{20}Ne$(n,\gamma)^{21}$Ne and ^{12}C(^{12}C, $p)^{23}$Na reactions [18]. Shortly after the explosion low-density graphite grains are formed in the expanding

*corresponding author: m.heil@gsi.de
[†]NuGrid collaboration, http://www.nugridstars.org

ejecta (e.g., [19]). In-situ decay of ^{22}Na contained in these grains is responsible for the ^{22}Ne anomalies of the Ne-E(L) component.

In view of these questions, the (n,γ) cross sections of all stable Ne isotopes have been investigated with improved accuracy. Resonance analyses were carried out using experimental data in the neutron energy range between 5 and 230 keV, which had previously been evaluated only in terms of averaged cross sections [2]. Resonance information is particularly useful for ^{21}Ne, where these data are missing so far. In case of ^{20}Ne and ^{22}Ne the present work complements previous time-of-flight (TOF) results [3, 6] and adds to the analysis of activation measurements in quasi-stellar neutron spectra [4, 5].

The cross section data and the resonance analysis are described in Secs. II and III. Sec. IV deals with the determination of the additional components from the direct radiative capture (DRC) channels. In Sec. VI the final Maxwellian averaged cross sections (MACS) are compared with the recommended values in the KADoNiS data base [20, 21] (www.kadonis.org). The effect of the new stellar cross sections on the *s*-process in thermally pulsing low-mass asymptotic giant branch (AGB) stars and in massive stars is discussed in Sec. VII.

II. CROSS SECTION DATA

The total cross sections as well as the capture cross sections used in this study were measured 30 years ago at the Karlsruhe Van de Graaff accelerator using the TOF technique [2, 22]. Neutrons were produced via the ^{7}Li(p,n)^{7}Be reaction by bombarding a metallic target of natural Li with a pulsed proton beam of 1.0 ns burst width and a variable repetition rate of 1 MHz and 250 kHz for the capture and transmission runs, respectively.

The total cross sections of all three isotopes were determined between 5 keV and 800 keV in a common transmission measurement. The samples consisted of highly enriched neon gas (99.8% ^{20}Ne, 95.4% ^{21}Ne, and 99.8% ^{22}Ne) contained in stainless steel cylinders at a pressure of 150 atmospheres. The cylinders were 100 mm in length and 28 mm in diameter, with 0.5 mm thick walls. The three samples were mounted on a sample changer together with an empty container for background determination. Neutrons were detected via the ^{10}B(n,α)^{7}Li* reaction, using two deuterated benzene (C_6D_6) liquid scintillation detectors for registration of the 478 keV γ-rays of the ^{7}Li ground state transition. The overall resolution was determined by the time resolution of the detectors (0.6 ns) and of the proton pulse (1.0 ns), resulting in a TOF resolution of 0.4 ns/m. Because of the 3 m flight path, the repetition rate of the accelerator was reduced to 250 kHz in order to avoid overlap problems. Under these conditions a resolution in neutron energy of 0.6% and 1.8% could be achieved at neutron energies of 30 keV and 300 keV, respectively.

For the capture cross section measurement the setup was modified by using a well collimated neutron beam at a shorter flight path of 60 cm, and a higher repetition rate of 1 MHz. The sample containers were compact stainless steel spheres 20 mm in diameter and 0.5 mm in wall thickness. The spheres were filled through a thin neck with the more massive valve remaining outside the neutron beam to minimize the effect of scattered neutrons. With these spheres, the signal-to-background ratio could be improved by increasing the gas pressure to 300 atmospheres. Neutron capture events were detected via the prompt γ-ray cascade, using the C_6D_6 detectors in combination with the pulse height weighting technique. Backgrounds were determined from spectra taken with an empty gas cell and an empty position on the sample ladder. The neutron flux was determined relative to a gold sample, which served as a cross section standard. The capture experiment was performed in the neutron energy range between 5 and 230 keV.

At the time of the measurement, the (n,γ) cross sections of the Ne isotopes were predicted to be of the order of a few millibarns [23]. Since the carefully optimized experimental setup was designed for a sensitivity of better than one millibarn, it was attempted to determine the stellar cross sections directly via the small difference in the spectra obtained with the Ne samples and the corresponding backgrounds, instead of going through a detailed resonance analysis.

Although the experimental sensitivity was expected to provide reliable data down to cross sections of a few millibarns, a posteriori this approach was prone to fail because the MACS values are actually in the μb range and mostly determined by the very small, but continuous DRC components and not by the few resonances. Accordingly, the background subtraction became a crucial problem, resulting in a severe overestimation of the capture cross sections.

In fact, later TOF measurements with better resolution had found no convincing evidence for resonances in ^{22}Ne [3]. Furthermore, activation measurements in the keV region [4, 5] showed that the ^{22}Ne(n,γ) cross section could be described by the value at thermal energy and a 1/v slope, consistent with theoretical estimates for an s-wave component of the DRC channel [24]. Compared to these results, the data analysis of Ref. [22] had overestimated the cross section by at least an order of magnitude. Similar discrepancies were found for ^{20}Ne and ^{21}Ne, where a 1/v extrapolation of the thermal cross sections also indicated much lower cross sections in the keV region.

While the activation results helped to settle the role of ^{22}Ne as a neutron poison in the *s*-process [5], an increasing body of information on isotopic abundance patterns in presolar SiC grains [15, 25] as well as the persisting Ne(E) problem related to the production of ^{22}Na in explosive scenarios [26] called for a re-analysis of the existing neutron TOF data [22].

III. RESONANCE ANALYSIS

The resonances in the capture cross sections were identified and analyzed using the multilevel R-matrix code SAMMY [27]. The fitting procedure applied in SAMMY to find the best fit values of parameters and the associated parameter covariance matrix is based on the Bayes theorem. Corrections to the experimental data, i.e. for self-shielding, multiple scattering, and sample impurities were already included in the cross section analysis of Ref. [2] and are globally considered by the overall systematic uncertainty of 7%. Therefore, only the experimental resolution was used in the SAMMY fits. The actual results are illustrated in Figs. 1 to 3 by comparison with the measured data.

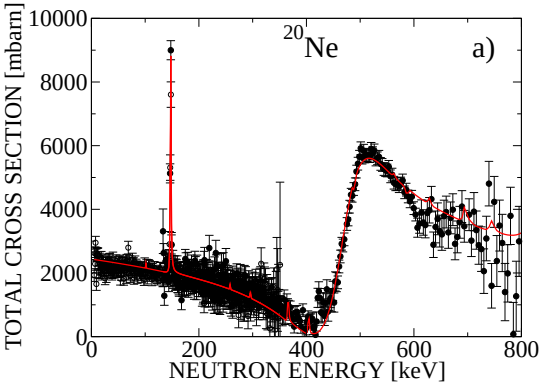

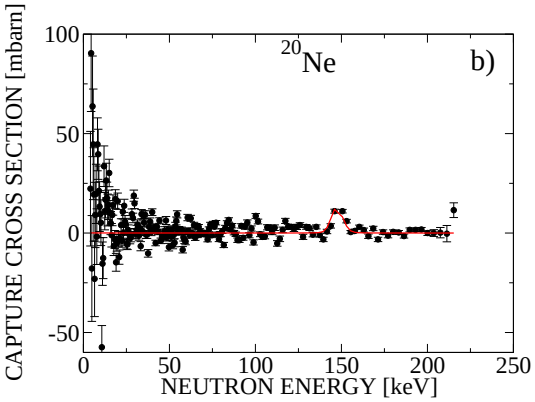

FIG. 1: Color online. (a) Total cross section of ^{20}Ne obtained from the measured transmission data and the corresponding $\mathcal{R}$-matrix fit. (b) The capture data contain only one significant resonance at 147 keV neutron energy.

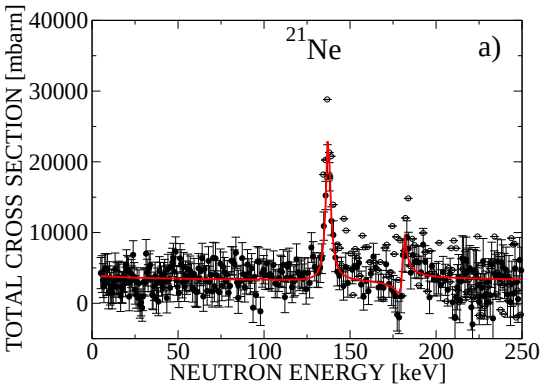

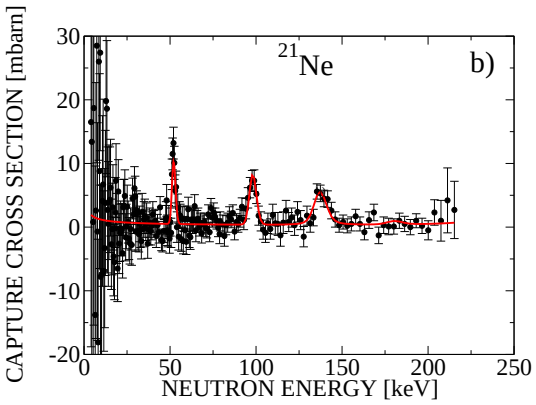

FIG. 2: Color online. Same as Fig. 2 but for ^{21}Ne. For this isotope, three capture resonances at 52, 98, and 137 keV could be identified.

The SAMMY fits provided the capture kernels

$$A_\gamma = g\frac{\Gamma_n \cdot \Gamma_\gamma}{(\Gamma_n + \Gamma_\gamma)} \qquad (1)$$

which represent the integral over the resonance area. The accuracy of the capture kernels is essentially limited by the counting statistics, resulting in overall uncertainties between 6 and 15% in most cases.

The kernels are determined by the capture and neutron widths, Γ_n, Γ_γ, and by the statistical spin factors

$$g = \frac{(2J+1)}{(2I_n+1)(2I_{\rm Ne}+1)},$$

containing the resonance spins, J, the neutron spin I_n=1/2, and the spin of the target nuclei. Individual values for the capture width Γ_γ could be determined only

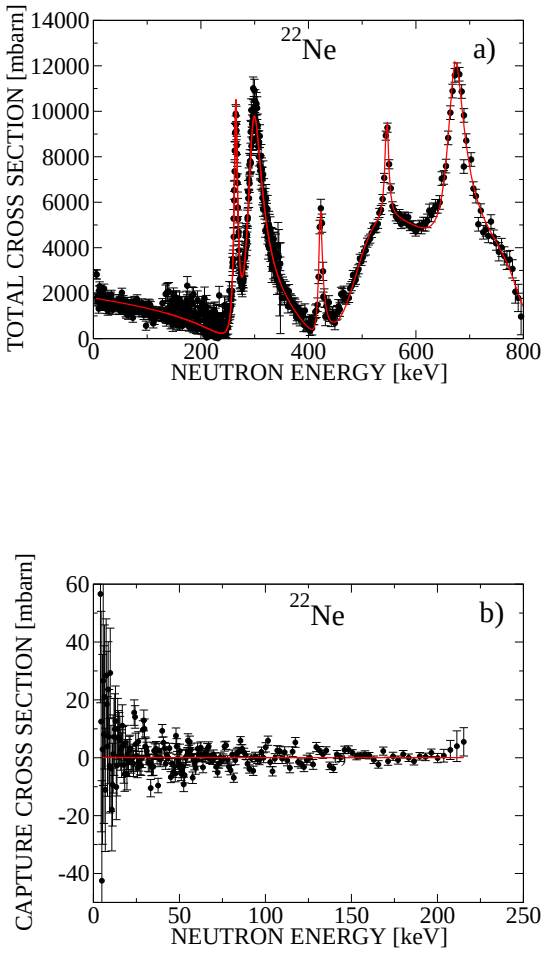

FIG. 3: Color online. Same as Fig. 2 but for ^{22}Ne. No resonances were found below 230 keV.

for those resonances, which were observed in the total cross section as well.

The information on J and ℓ assignments from Ref. [28] for the two resonances in ^{20}Ne as well as for the first four resonances in ^{22}Ne could be confirmed by the present SAMMY fits. In case of the ^{22}Ne resonances at 564 and 690 keV different J and ℓ values are proposed, however. The corresponding values for the resonances in ^{21}Ne and for the 802 keV resonance in ^{22}Ne, which are reported for the first time, were determined by the SAMMY fits.

The resonance energies are given with uncertainties of $\pm 1\%$ corresponding to the accuracy in the experimental definition of the flight path in the transmission measurements. Exceptions are the ^{21}Ne resonances at 52.1 and 98.2 keV, which do not appear in the total cross section; their energy uncertainties are five times larger due to the 60 cm flight path in the capture measurements. The only case, where the statistical uncertainty was limiting the energy determination is the weak ^{21}Ne resonance at 180.6 keV. Resonances seen only in the total cross sections have been included in Table I, because this information is missing in literature so far. These cases are almost negligible in astrophysical applications, however.

The comparison in Table I summarizes all resonance information presently available in the astrophysically relevant energy region. The strength of the only resonance in ^{20}Ne at 147 keV has been found to be 80% larger than reported by Winters and Macklin [3]. A possible reason could be the higher signal-to-background ratio obtained in the experiment of Ref. [2], where the mass ratio of ^{20}Ne and of the stainless steel container was two times larger.

The resonance parameters for the capture channel in ^{21}Ne are reported for the first time. Except for the weak resonance at 180 keV, the kernels could be determined with statistical uncertainties around 10%. A possible subthreshold resonance at -7.6 keV [28] has been omitted in the SAMMY analysis. Instead, the thermal cross section has been assumed to be dominated by the direct radiative capture (DRC) channel as discussed in the following section. In any case, the effect of that resonance would be small compared to the overall uncertainties of the stellar cross sections presented in Sec. VI.

In the capture cross section of ^{22}Ne no resonances were found in the investigated energy range below 200 keV. Above, resonance energies and neutron widths have been determined by the SAMMY analysis of the total cross section. The contribution of these resonances to the stellar capture rate (Table V) was constrained by the experimental MACS values at $kT = 25$ and 52 keV [4, 5] as discussed in Sec. VI. Accordingly, the capture widths in Table I are four times smaller than in Ref. [28]. The resonance energies could be improved because of the good energy resolution of the total cross section measurement.

IV. DIRECT RADIATIVE CAPTURE

The γ decay of the capturing states to low-lying states in the product nuclei via the DRC mechanism represents an important non-resonant contribution to the stellar Ne cross sections, particularly for the even isotopes.

The s-wave part of the DRC components is essentially represented by the thermal (n,γ) cross sections. Therefore, the s-wave part was described by a 1/v extrapolation of the thermal cross sections, corrected for the small contribution from the tails of the few resonances in the keV energy range. The thermal cross sections of ^{20}Ne and ^{21}Ne exhibit uncertainties of 11% and 17%, respectively. Only for ^{22}Ne, where DRC dominates the MACS values in the entire energy region of relevance for the s process, an accurate thermal cross section, $\sigma_{th} = 52.7 \pm 0.7$ mb has recently been measured by the activation technique [30]. For ^{20}Ne and ^{21}Ne, the calculated DRC results were found in good agreement with the thermal cross sections

TABLE I: Resonance parameters obtained in this work (in eV) compared to previous data.

Resonance energy (keV)	J	ℓ	This work Γ_γ	This work Γ_n	This work g	This work A_γ^1	Refs. [28, 29] Γ_γ	Refs. [28, 29] $g\Gamma_n$
				^{20}Ne(n,γ)				
147.40±0.15	1/2	1	3.7±0.2	861±29	1/3		2.016±0.256	319±67
472.6±0.5	1/2	0		107795±1113	1			
				^{21}Ne(n,γ)				
52.1±0.3	4	2			9/10	0.28±0.03		
98.2±0.5	4	2			9/10	0.72±0.09		
137.3±0.2	4	2	1.56±0.21	3157±240	9/10			
180.6±0.4	2	0	< 0.24	2236±568	5/2			
				^{22}Ne(n,γ)				
272.0±0.3	1/2	1	(200)[2]	8226±190	1/3			4200
290.7±0.3	1/2	0	(200)	28609±471	1		0.84	34700
427.1±0.5	1/2	1	(200)	8204±311	1/3			
493.1±0.5	1/2	0	(200)	118795±2147	1			
564.1±0.6	3/2	2	(200)	51008±180	4/10			
690.4±0.7	3/2	1	(200)	37457±1122	7/10			
802±5	1/2	0	(200)	27184±5139	1			

[1] Capture kernel $A_\gamma = g\Gamma_n\Gamma_\gamma/(\Gamma_n + \Gamma_\gamma)$.
[2] Γ_γ values of ^{22}Ne resonances adjusted to fit experimental MACS values (Sec. VI).

TABLE II: Wood-Saxon parameters used in the calculation of the bound state and scattering wave functions.

Radius parameter r_0= 1.2360 fm Diffuseness d = 0.62 fm Spin-orbit strength V_{so}= 7.0 MeV			
nlj	B_n (MeV)	J_f^1	Well depth V_0(MeV)
^{21}Ne bound states			
1d5/2	6.4110	2.5	49.9
2s1/2	3.9670	0.5	
^{22}Ne bound states			
1d5/2	9.0890	2.0	51.0
2s1/2	5.0050	2.0	
1d5/2	4.8480	2.0	
2s1/2	3.5430	2.0	
2s1/2	3.5060	1.0	
1d5/2	2.2230	2.0	
1d5/2	1.8160	2.0	

[1] Total spin of final state.

and have been directly used in Tables III and IV.

The capturing states in ^{20}Ne, ^{21}Ne, and ^{22}Ne can also decay to low-lying $1/2^+$, $3/2^+$, and $5/2^+$ states in the respective product nuclei, giving rise to additional p-wave DRC components. Except in the work by Tomyo *et al.* [6] these p-wave contributions, which are increasing with $\sqrt{E_n}$, were not considered in previous analyses.

The p-wave components have been calculated using the potential two-body model with bound-state wave functions determined by a Woods-Saxon mean-field potential with fixed well depth parameters to reproduce the experimental binding energy B_n (Table II).

With that model, the DRC cross sections were obtained by determining the overlap integral of the bound-state wave functions with the continuum wave functions. The latter were derived from the scattering matrix elements (phase shifts) for a mean-field potential with the same geometrical parameters. The available values for the scattering lengths [28] correspond to mean-field potentials $V_0 = 49.9$ MeV for ^{20}Ne and 51.0 MeV for ^{21}Ne.

The uncertainties of the p-wave calculations are determined by the spectroscopic factors and by the model parameters used to calculate the wave functions for the continuum. The first component is proportional to the spectroscopic factors of the low-lying bound states populated by the direct transitions from p-wave neutrons captured in the continuum, which are typically affected by uncertainties of 15-20%. The second component due to the model parameters is estimated to contribute an uncertainty of 20% by varying the strength of the mean field potential by 2 MeV. Accordingly, a total uncertainty of 30% is adopted for the calculated p-wave components of the MACS data of ^{20}Ne and ^{21}Ne.

For ^{22}Ne, the p-wave component has been calculated assuming unity for all spectroscopic factors involved, because the data obtained in activation measurements [4, 5] could be used for normalization. Within the 30% uncertainty estimated for the calculation of the p-wave components, the normalization factor of 0.37 ± 0.04 turned out to be consistent with the full DC calculation as the respective spectroscopic factors fall in the range 0.07 - 0.7 with an average value of 0.29 [31].

V. STELLAR (n,γ) CROSS SECTIONS

The resonance contributions obtained with SAMMY and the DRC contributions described above are summarized in Tables III - V for thermal energies between $kT = 5$ and 100 keV, and the resulting MACS values are compared with the recommended MACS values in the KADoNiS compilation [5, 21].

In general, the conversion of experimental data into stellar cross sections requires a correction, the so-called stellar enhancement factor (SEF), in order to account for the effect of the high temperatures at the various *s*-process sites, which give rise to thermal equilibrium in the population of excited nuclear states. The possible contribution of excited states to the stellar reaction rate has to be evaluated by theory. In the case of the stable Ne isotopes, however, the SEF corrections can be neglected, because the excited states are too high in energy to be significantly populated [32].

In case of ^{20}Ne and ^{21}Ne, the resonances contribute substantially to the MACS values in the temperature range of the *s*-process scenarios, in particular above $kT = 20$ keV. Accordingly, it is important to note that - apart from the 147 keV resonance in ^{20}Ne [28, 29] - all capture resonances below 200 keV have been determined for the first time.

The stellar (n,γ) cross section of ^{20}Ne is significantly larger than previously recommended [21] on the basis of the data by Winters and Macklin [3]. The difference is essentially due to the revised strength of the resonance at 147 keV (Table III).

The MACS of ^{21}Ne could be considerably improved. Below $kT = 20$ keV the stellar cross sections are determined by the s-wave DRC component, but at higher kT the values are clearly dominated by the contributions from the resonance information obtained in the present analysis as shown in Table IV. In contrast to the compilation of Ref. [21], where only few data could be estimated based on the uncertain values of Ref. [2], the present set of MACS data covers the entire range of *s*-process temperatures with considerably reduced uncertainties.

The quoted MACS uncertainties are composed of the contributions from the DRC components and from the resonances. The DRC uncertainties discussed above have been treated as systematic uncertainties. Accordingly, the total systematic uncertainties of the MACS data are the sum of these components and of the 7% uncertainty quoted in Ref. [2] for the systematics of the experiment. These values were then added in quadrature to the statistical uncertainties of the resonance contributions given in the second columns of Tables III - V.

For both, ^{20}Ne and ^{21}Ne, the uncertainties are dominated by the DRC part up to $kT \approx 25$ keV, where the resonances start to contribute significantly.

The experimental MACS values of ^{22}Ne for $kT = 25$ and 52 keV from the activation measurements of Beer *et al.* [4, 5] represent important constraints for the relative contributions from DRC and from the resonances at higher energies (Table V). The dominant s-wave component of the DRC channel has been normalized using the thermal capture cross section of 52.7 ± 0.7 mb of Belgya *et al.* [30].

The p-wave part of the DRC channel was neglected in Ref. [5] and the cross section excess above 100 keV was assigned to the tails of the resonances above 250 keV. According to our calculations, however, the p-wave part contributes significantly at higher energies. While the s-wave component is defined by the thermal point and the MACS value of 66±5 μb measured at $kT = 25$ keV [4], the p-wave part can be constrained by the MACS value of 43.0±4.8 μb at $kT = 52$ keV [5], where the resonance contributions are still small. A best fit based on the experimental data points at thermal as well as at $kT = 25$ and 52 keV yields the MACS values listed in Table V. The quoted uncertainties of these values are essentially determined by the dominant DRC components. Systematic uncertainties of 3% and 10% were assigned to the s- and p-wave contributions, because the first could be normalized by means of the thermal cross section whereas the second had to rely on the measured MACS data at 25 and 52 keV. The small resonance contributions are estimated to carry uncertainties of about 30% according to the schematic Γ_γ assignments for the resonances above 270 keV in Table I.

Comparison of the present results with the recommended MACS values in KADoNiS [5, 21] in Table V shows that the new values are systematically lower. This holds in particular with respect to the measured data for the quasi-stellar spectrum at $kT = 52$ keV [4]. In order to match the spectrum averaged cross sections above 100 keV [5], large strengths for the high-energy resonances had been assumed by theoretical and likely very uncertain arguments (see [5] and references therein). However, if the p-wave part of the DRC channel is included, the resonance contributions are reduced by a factor of four, thus reconciling the MACS values with the experimental data points of Beer *et al.* [4, 5].

VI. ASTROPHYSICS

A. AGB stars

Thermally pulsing low-mass AGB stars are known to be responsible for the so-called *main* *s*-process component that constitutes about half of the observed abundances between Zr and Bi [1, 33, 34]. About 95% of the *s*-process production in these stars occurs in the rather quiescent periods between thermal pulses, where neutrons are provided via the ^{13}C$(\alpha,n)^{16}$O reaction in the ^{13}C pocket, a thin layer on top of the C/O core. This phase is characterized by thermal energies of $kT = 8$ keV and comparably low neutron densities of about 10^7 cm^{-3}. A second, smaller exposure is added during the subsequent thermal pulses, when the ^{22}Ne$(\alpha,n)^{25}$Mg reaction is marginally activated at temperatures of typically 250

TABLE III: Resonance and DRC contributions to the MACS of ^{20}Ne (all values in (μb).

kT (keV)	Resonances[1]	DRC contributions		Total MACS	
		s-wave[2]	p-wave[3]	This work[4]	KADoNiS [21]
5	0.3±0.02	70.9	14.2	85±12	88
8	0.4±0.03	56.0	18.0	74±12	
10	0.7±0.04	50.1	20.1	71±12	62
15	7.4±0.4	40.9	24.7	73±12	53
20	39±3	35.4	28.6	103±16	60
23	73±4	33.0	30.7	137±18	
25	100±6	31.7	32.0	164±21	84
30	176±11	28.9	35.1	240±29	119±11
40	318±19	25.1	40.7	384±42	191
50	411±25	22.4	45.6	479±52	242
60	456±27	20.5	50.1	527±56	259
80	460±28	17.7	58.1	536±59	272
90	442±27	16.7	61.8	521±58	
100	419±25	15.8	65.2	500±56	253

[1]Statistical uncertainties are 6%.
[2]Uncertainty of 11% from normalization to thermal cross section.
[3]Adopted uncertainty 30% (see text).
[4] Including 7% systematic uncertainty of the experiment [2].

TABLE IV: Resonance and DRC contributions to the MACS of ^{21}Ne (all values in (μb).

kT (keV)	Resonances[1]	DRC contributions		MACS	
		s-wave[2]	p-wave[3]	This work[4]	KADoNiS [21]
5	3.2±0.4	1428	9	1440±244	
8	51±7	1129	12	1192±200	
10	115±13	1010	13	1138±184	
15	301±31	825	16	1142±169	
20	458±42	714	19	1191±164	1700
23	534±49	666	21	1221±163	
25	576±53	639	21	1236±163	1600
30	656±50	583	24	1263±160	1500±900
40	727±52	505	28	1260±154	1300
50	725±52	452	31	1208±147	1200
60	687±50	412	34	1133±137	
80	578±44	357	40	975±121	
90	526±40	337	43	906±114	
100	477±37	319	46	842±108	

[1]Statistical uncertainties are 8 - 10%.
[2]Uncertainty of 17% from normalization to thermal cross section.
[3]Adopted uncertainty 30% (see text).
[4] Including 7% systematic uncertainty of the experiment [2].

Million K ($T_8 = 2.5$), resulting in peak neutron densities up to a few 10^{11} cm^{-3}.

The impact of the new MACS values for the final abundance distribution of the main *s* component has been investigated following the prescription of Ref. [34]. The analysis was carried out by averaging the results obtained with AGB stellar models of initial masses M = 1.5 and 3 M$_\odot$, a metallicity [Fe/H] = −0.3, and a specific choice for the ^{13}C-pocket. This approximation, which has been shown to reproduce the main *s* component in the solar system quite well [34], was adopted because it provides a useful test for investigating the effect of nuclear cross sections in general.

The analysis was made by calculating the *s* abundances of the main component using the compiled MACS values from the KADoNiS data base [21]. This abundance distribution was then compared with the results obtained with the new MACS values. From the comparison of the two distributions one finds that the isotopic abundances of the main component show differences of less than 2-3%, indicating that neon represents only a feeble neutron poison. This was confirmed in subsequent tests assuming MACS = 0 for ^{20}Ne, ^{21}Ne, and ^{22}Ne, respectively. While the first two cases produced negligible effects, differences

TABLE V: Resonance and DRC contributions to the MACS of ^{22}Ne (all values in (μb).

kT (keV)	Resonances[1]	DRC contributions		Total MACS		Exp. data
		s-wave[2]	p-wave[3]	This work	KADoNiS [21]	
5	2.8	105.4	0.9	109.1±4.1	133±9	
8	2.3	83.3	4.0	88.8±3.6	106±7	
10	2.1	74.5	4.5	81.1±3.3	95±6	
15	1.9	60.9	5.6	68.4±3.0	78±5	
20	1.7	52.7	6.5	60.9±2.8	68±4	
23	1.7	49.1	7.1	57.9±2.7		
25	1.8	47.1	7.4	56.3±2.6	62±4	66±5 [4]
30	2.0	43.0	8.2	53.2±2.7	58±4	
40	3.2	37.3	9.7	50.2±3.1	56±5	
50	5.5	33.3	11.0	49.8±3.8	61±7	
52	6.0	32.7	11.2	49.9±3.8		43.0±4.8 [5]
60	8.1	30.4	12.3	50.8±4.5	69±11	
80	13.3	26.4	14.8	54.5±6.3	85±17	
90	15.5	24.8	15.9	56.2±7.0	90±19	
100	17.3	23.6	17.0	57.9±7.6	95±21	

[1] Using radiative widths of Table I.
[2]Uncertainty of 3% from normalization to thermal cross section.
[3]DRC calculation normalized at $kT = 52$ keV by factor 0.366 ± 0.037 (see text).

up to 10% were found for the third case, emphasizing that the poisoning effect is limited to ^{22}Ne. For the neon abundances themselves, the new MACS values had a significant effect only for the odd isotope ^{21}Ne as illustrated in Table VI. On average, the uncertainties could be reduced by factors of two to five.

TABLE VI: Comparison of neon overabundances produced by the main s component calculated with the present MACS values and with previously recommended data [21].

Isotope	s-Process overabundances[1]		Ratio
	KADoNiS [21]	This work	
^{20}Ne	1.04 10^{-3}	1.01 10^{-3}	0.97
^{21}Ne	5.55 10^{-3}	6.20 10^{-3}	1.12
^{22}Ne	2.10 10^{-1}	2.04 10^{-1}	0.97

[1]Numbers are normalized at ^{150}Sm and are given relative to solar values.

B. Meteoritic Ne-E(H) and SiC grains

With the new MACS values it is also possible to improve the predictions for the pure s-process components of the Ne isotopes with updated AGB models of solar metallicity [35]. Using the prescription outlined in Ref. [1] we considered only the advanced thermal pulses when C/O≥1, because SiC grains are only forming in the carbon-enriched stellar winds [36]. Note that partial He burning during a thermal pulse produces primary ^{12}C, which is mixed to the envelope by third dredge-up episodes, thus gradually increasing the C abundance, while oxygen remains unchanged.

As shown in Ref. [1], the abundance patterns of SiC grains are best fit with half the mean neutron exposure that is needed to describe the main s component in the solar system. Accordingly, the predicted ^{20}Ne/^{22}Ne and ^{21}Ne/^{22}Ne ratios in SiC grains were calculated for AGB models at [Fe/H] = 0, initial masses M = 1.5, 2, and 3 M$_\odot$, and assuming the standard ^{13}C-pocket [1], which corresponds to a mean neutron exposure $\tau_0 \approx 0.15$ mbarn^{-1}. The results listed in Table VII were obtained by averaging over the last 6, 11, and 13 pulses of the 1.5, 2, and 3 M$_\odot$ models, respectively.

TABLE VII: Neon isotopic ratios expected for SiC grains[1].

Mass (M$_\odot$)		KADoNiS [21]	This work	Ratio
1.5	^{20}Ne/^{22}Ne	6.98 10^{-2}	6.97 10^{-2}	1.00
	^{21}Ne/^{22}Ne	9.33 10^{-4}	1.05 10^{-3}	1.13
2.0	^{20}Ne/^{22}Ne	7.70 10^{-2}	7.68 10^{-2}	1.00
	^{21}Ne/^{22}Ne	9.41 10^{-4}	1.06 10^{-3}	1.13
3.0	^{20}Ne/^{22}Ne	6.87 10^{-2}	6.85 10^{-2}	1.00
	^{21}Ne/^{22}Ne	8.49 10^{-4}	1.00 10^{-3}	1.17
Average	^{20}Ne/^{22}Ne	7.18 10^{-2}	7.17 10^{-2}	1.00
	^{21}Ne/^{22}Ne	9.08 10^{-4}	9.96 10^{-3}	1.14

[1]Considering only advanced thermal pulses with C/O≥1.

The surface abundance ratios obtained with the present MACS results are 0.072(9) for ^{20}Ne/^{22}Ne and 0.0010(2) for ^{21}Ne/^{22}Ne, the quoted uncertainties referring only to the MACS contributions. These ratios were found to decrease by less than 10% if the metallicity in the investigated models was reduced by a factor of two.

The results of Table VII are slightly different from earlier predictions [14], but exhibit considerably improved accuracy. This holds also for results that have been obtained with recent AGB models by Cristallo *et al.* [37] and by Karakas [38].

Comparison of these predictions with measured isotopic anomalies in meteoritic SiC grains provides a more accurate analysis for the Ne-E(H) component as summarized by Hoppe and Ott [39]. For the Murchison meteorite, the measured ^{20}Ne/^{22}Ne and ^{21}Ne/^{22}Ne ratios are 0.0827(18) and 0.00059(10), respectively. The differences between AGB predictions and the observed Ne-E(H) component have been interpreted due to the modification of the pure *s*-process pattern by cosmic-ray spallation [12, 15, 40]. Once SiC grains are shielded from cosmic rays inside meteorites, these differences are characteristic of their residence time in interstellar space. In this respect, ^{21}Ne is most sensitive to the cosmic-ray age because of its very low abundance. The discussion of inferred exposure ages, which have been estimated to range from 10 to 130 million years depending on grain size [40–42], may strongly benefit from the present cross section data.

C. Massive stars

Massive stars (M > 10 M$_\odot$) are known to produce most of the *s*-process abundances in the solar system between Fe and Sr (weak *s*-process component, [35] and references therein). The neutron exposure starts in the convective He core, but only in the last phase, close to He exhaustion, when the temperature is high enough for the ^{22}Ne$(\alpha,n)^{25}$Mg channel. The ^{22}Ne source for the weak *s* process corresponds to the initial CNO abundance because it has been formed by α captures on ^{14}N, which corresponds to the initial CNO abundances. At the point of He exhaustion the most abundant isotopes are ^{16}O, ^{12}C, ^{20,22}Ne and ^{25,26}Mg.

The neutron exposure in the convective C shell starts with C ignition at the bottom of the shell, where neutrons are mainly produced again by the ^{22}Ne$(\alpha,n)^{25}$Mg reaction. Typical temperatures at the bottom of the C shell are $T \approx 10^9$ K, possibly increasing in the last day(s) before the supernova (SN) explosion, and the peak neutron density is 10^{11}-10^{12} cm^{-3} (e.g., [7, 43]). At the end of the convective C-burning shell the most abundant isotopes are ^{16}O, ^{20}Ne, ^{23}Na and ^{24}Mg.

The impact of the new MACS values for the Ne isotopes on the weak *s* process in massive stars was investigated by means of a 25 M$_\odot$ model with an initial metal content Z = 0.02 [44]. The complete nucleosynthesis is followed by the post-processing NuGrid code MPPNP [45]. The abundance distributions between Fe and Mo, which were obtained with the previously recommended data in the KADoNiS compilation [21] and the new MACS reported in this work, are compared in Fig. 4.

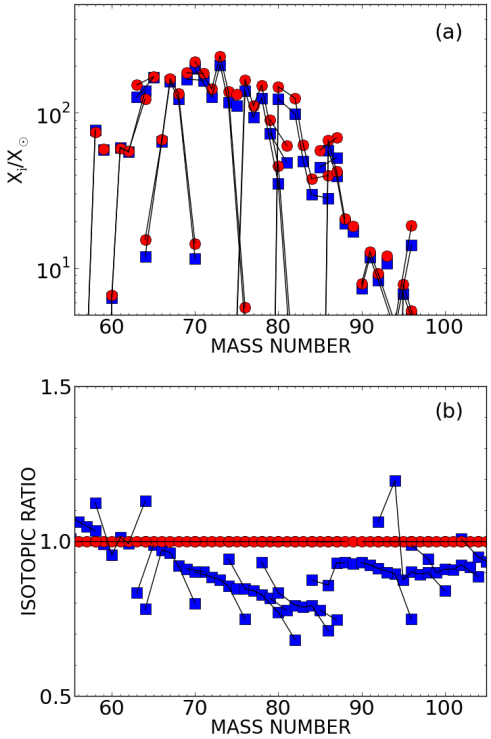

FIG. 4: Color online. (a) Calculated relative *s*-abundance distributions at the end of C shell burning for a 25 M$_\odot$ star. The results obtained with recommended data in the KADoNiS compilation [21] (red circles) are significantly modified when the MACS of ^{20}Ne, ^{21}Ne, and ^{22}Ne are replaced by the present values (blue squares). (b) Isotopic ratios emphasizing the enhanced neutron poison effect due to the larger MACS of ^{20}Ne from this work.

The *s*-process distribution based on an updated set of MACS values including the present results for the Ne isotopes exhibits a strong propagation effect and significantly reduced *s*-process yields, essentially due to the new larger cross section data for ^{20}Ne. While the Ni-Cu region is less affected as it is closer to the iron seed, the abundances of the heavier *s*-process nuclei are reduced by about 20% with maximum differences in the Kr-Rb region. At higher mass numbers the propagation effect is weakening because the *s*-process contributions in massive stars in general are strongly reduced above the Sr abundance peak.

The propagation effect, which is caused by the new MACS results for the Ne isotopes, is clearly reducing the efficiency of the weak *s* process. For a reliable description of the propagation effect, a number of MACS uncertainties remain to be resolved by new accurate cross section measurements. In addition to the light neutron poisons, this concerns especially the MACS values of less than 100 mbarn for the isotopes along the *s*-process path between Fe and Sr [7, 46–49].

Apart from the required neutron capture data, the de-

termination of the ^{22}Ne(α, n) rate represents one of the major challenges for experimental nuclear astrophysics (see Wiescher *et al.* [50] and references therein). The *s* process in massive stars is further affected by uncertainties in the triple α and the ^{12}C(α, γ) reactions [51] as well as in the ^{12}C+^{12}C channels [44, 45].

For the present analysis we considered a 25 $M_\odot$ star, where the *s*-process production is dominated by the convective C shell. Note that for stars of lower mass (e.g., for a 15 $M_\odot$ star) the *s*-process yields in the SN ejecta are likely to be more affected by the *s* process during convective core He-burning and convective shell He-burning. Consequently, the variations shown in Fig. 4 should be considered as an upper limit, because the MACS of ^{22}Ne around $kT = 25$ keV is almost unchanged, and ^{20}Ne is still a weak neutron poison at He-burning conditions.

This discussion underlines that the reproduction of the *s* abundances in the solar system are far from being settled. Better experimental data are clearly needed to improve the characterization of the *s*-process in massive stars (which can provide significant constraints for inherent uncertainties related to stellar models and to the SN explosion mechanisms) and to shed light on the problem of galactical chemical evolution calculations for reproducing the *s*-process elements [52].

VII. SUMMARY

Compared to the original data [2, 22] and to the recommended values of KADoNiS [21] the present resonance analysis shows that the MACS values of all Ne isotopes have to be revised. Although the newly analyzed resonances constitute a major part of the Maxwellian average at thermal energies around $kT = 30$ keV, the DRC contributions become increasingly important at lower temperatures, where most of the *s*-process neutron exposure occurs. In view of the rather large DRC uncertainties, this part should be improved by more accurate measurements of the thermal cross sections.

The consequences of the new MACS data for the Ne isotopes have been investigated for thermally pulsing, low-mass AGB stars, which are contributing the main *s*-process abundance component, essentially between Zr and Pb/Bi, as well as for massive stars, which are known to produce the weak *s* component from the Fe seed to Sr. With respect to the importance of the Ne isotopes as neutron poisons during the *s* process, AGB stars exhibit only a small effect, because the MACS value of the dominant isotope ^{22}Ne remained practically unchanged in the temperature window of the main component. In massive stars, however, the *s* abundances are reduced up to 20-30%, with the highest impact in the Kr-Rb region. Most of this effect comes from the higher MACS values of ^{20}Ne, which is abundantly produced during C shell burning. The enhanced role of ^{20}Ne as a neutron poison in massive stars and the consequences for the overall yields between Fe and Sr, and thus for Galactic chemical evolution, needs to be studied separately.

In addition to the neutron poison aspect, the new MACS data have led to improved predictions for the anomalous isotopic Ne patterns in presolar SiC grains, which are formed in the expanding ejecta of AGB stars.

Acknowledgements

MP acknowledges support from the Ambizione grant of the SNSF (Switzerland), from NSF grants PHY 02-16783 and PHY 09-22648 (Joint Institute for Nuclear Astrophysics, JINA) and EU MIRG-CT-2006-046520, and from EuroGENESIS (MASCHE). SB thanks JINA (Joint Institute for Nuclear Astrophysics) and KIT (Karlsruhe Institute of Technology, Germany) for financial support, and CL acknowledges support from the Austrian Science Fund (FWF): J3503.

[1] R. Gallino, C. Arlandini, M. Busso *et al.*, Ap. J. **497**, 388 (1998).
[2] J. Almeida and F. Käppeler, Ap. J. **265**, 417 (1983).
[3] R. Winters and R. Macklin, Ap. J. **329**, 943 (1988).
[4] H. Beer, G. Rupp, F. Voss, and F. Käppeler, Ap. J. **379**, 420 (1991).
[5] H. Beer, P.V. Sedichev, W. Rochow *et al.*, Nucl. Phys. **A 705**, 239 (2002).
[6] A. Tomyo, Y. Nagai, Y. Nobuhara *et al.*, Nucl. Phys. A **718**, 527 (2003).
[7] M. Pignatari, R. Gallino, M. Heil *et al.*, Ap. J. **710**, 1557 (2010).
[8] M. Pignatari, R. Gallino, G. Meynet *et al.*, Ap. J. **687**, L95 (2008).
[9] D. Black and R. Pepin, Earth Planet. Sci. Lett. **6**, 395 (1969).
[10] D. Black, Geochim. Cosmochim. Acta **36**, 377 (1972).
[11] T. Bernatowicz, G. Fraundorf, M. Tang *et al.*, Nature **330**, 728 (1987).
[12] M. Tang and E. Anders, Geochim. Cosmochim. Acta **52**, 1235 (1988).
[13] S. Amari, Ap. J. **690**, 1424 (2009).
[14] R. Gallino, M. Busso, G. Picchio, and C. Raiteri, Nature **348**, 298 (1990).
[15] R. Lewis, S. Amari, and E. Anders, Nature **348**, 293 (1990).
[16] U. Ott and F. Begemann, Meteoritics and Planetary Sciences **35**, 53 (2000).
[17] S. Amari, E. Anders, A. Virag, and E. Zinner, Nature **345**, 238 (1990).
[18] S. Amari, R. Gallino, M. Limongi, and A. Chieffi, in *Origin of matter and evolution of galaxies*, edited by S.

Kubono *et al.* (AIP, New York, 2006), p. 311, aIP Conference Proceedings, Vol. 847.
[19] S. Colgan, M. Haas, E. Erickson *et al.*, Ap. J. **427**, 874 (1994).
[20] Z. Bao, H. Beer, F. Käppeler *et al.*, Atomic Data Nucl. Data Tables **76**, 70 (2000).
[21] I. Dillmann, R. Plag, F. Käppeler, and T. Rauscher, in *EFNUDAT Fast Neutrons - scientific workshop on neutron measurements, theory & applications*, edited by F.-J. Hambsch (JRC-IRMM, Geel, 2009), pp. 55 – 58, http://www.kadonis.org.
[22] J. Almeida, Report KFK-3347, Forschungszentrum Karlsruhe (1982).
[23] S. Woosley, W. Fowler, J. Holmes, and B. Zimmerman, Atomic Data Nucl. Data Tables **22**, 371 (1978).
[24] M. Wiescher, private communication (unpublished).
[25] E. Zinner, M. Tang, and E. Anders, Geochi. Cosmochim. Acta **53**, 3273 (1989).
[26] S. Amari and E. Zinner, Nucl. Phys. A **621**, 99c (1997).
[27] N. Larson, Updated Users Guide for SAMMY: Multilevel Rmatrix Fits to Neutron Data Using Bayes Equations, Report ORNL/TM-9179/R5, Oak Ridge National Laboratory (2000).
[28] S. Mughabghab, in *Atlas of Neutron Resonances, 5^{th} Edition* (Elsevier, Amsterdam, 2006).
[29] S. Sukhoruchkin, Z. Soroko, and V. Deriglazov, *Landolt–Börnstein New Series, Group I, Vol. 16, Subvolume B* (Springer, Berlin, 1998).
[30] T. Belgya, E. Uberseder, D. Petrich, and F. Käppeler, in *Capture Gamma-Ray Spectroscopy and Related Topics*, edited by A. Blazhev, J. Jolie, N. Warr, and A. Zilges (AIP, New York, 2009), p. 367.
[31] J.K. Tuli, Evaluated Nuclear Structure Data File (ENSDF), Brookhaven National Laboratory (2014), http://www.nndc.bnl.gov/ensdf/.
[32] T. Rauscher, P. Mohr, I. Dillmann, and R. Plag, Ap. J. **738**, 143 (2011).
[33] M. Busso, R. Gallino, and G. Wasserburg, Ann. Rev. Astron. Astrophys. **37**, 239 (1999).
[34] C. Arlandini, F. Käppeler, K. Wisshak *et al.*, Ap. J. **525**, 886 (1999).
[35] F. Käppeler, R. Gallino, S. Bisterzo, and W. Aoki, Rev. Mod. Phys. **83**, 157 (2011).
[36] E. Zinner, Ann. Rev. Earth Planet. Sci. **26**, 147 (1998).
[37] S. Cristallo, O. Straniero, R. Gallino *et al.*, Ap. J. **696**, 797 (2009).
[38] A. Karakas, Mon. Not. Royal Astron. Soc. **403**, 1413 (2010).
[39] P. Hoppe and U. Ott, in *Astrophysical Implications of the Laboratory Study of Presolar Material*, edited by T. Bernatowitz and E. Zinner (AIP, New York, 1997), p. 27.
[40] R. Lewis, S. Amari, and E. Anders, Geochim. Cosmochim. Acta **58**, 471 (1994).
[41] U. Ott, P. Heck, F. Gyngard *et al.*, PASA **26**, 2970 (2009).
[42] P. Heck, F. Gyngard, U. Ott *et al.*, Ap. J. **698**, 1155 (2009).
[43] L. The, M. El Eid, and B. Meyer, Ap. J. **655**, 1058 (2007).
[44] M. Pignatari, R. Hirschi, M. Wiescher, *et al.*, Ap. J. **762**, 31 (2013).
[45] M. Bennett, R. Hirschi, M. Pignatari *et al.*, Mon. Not. Royal Astron. Soc. **420**, 3047 (2012).
[46] H. Nassar, M. Paul, I. Ahmad *et al.*, Phys. Rev. Lett. **94**, 092504 (2005).
[47] M. Heil, F. Käppeler, E. Uberseder *et al.*, Phys. Rev. C **77**, 015808 (2008).
[48] J. Marganiec, I. Dillmann, C. Domingo Pardo *et al.*, Phys. Rev. C **79**, 065802 (2009).
[49] R. Reifarth, S. Dababneh, M. Heil *et al.*, Phys. Rev. C **85**, 035802 (2012).
[50] M. Wiescher, F. Käppeler, and K. Langanke, Ann. Rev. Astron. Astrophys. **50**, 165 (2012).
[51] C. Tur, A. Heger, and S. Austin, Ap. J. **702**, 1068 (2009).
[52] C. Travaglio, R. Gallino, E. Arnone *et al.*, Ap. J. **601**, 864 (2004).